

A Novel Breast Ultrasound Image Augmentation Method Using Advanced Neural Style Transfer: An Efficient and Explainable Approach

Lipismita Panigrahi, Prianka Rani Saha, Jurdana Masuma Iqrah, Sushil Prasad

The University of Texas at San Antonio
lipismita.panigrahi@utsa.edu
priankarani.saha@my.utsa.edu,
jurdanamasuma.iqrah@utsa.edu,
sushil.prasad@utsa.edu

Abstract

Clinical diagnosis of breast malignancy (BM) is a challenging problem in the recent era. In particular, Deep learning (DL) models have continued to offer important solutions for early BM diagnosis but their performance experiences overfitting due to the limited volume of breast ultrasound (BUS) image data. Further, large BUS datasets are difficult to manage due to privacy and legal concerns. Hence, image augmentation is a necessary and challenging step to improve the performance of the DL models. However, the current DL-based augmentation models are inadequate and operate as a black box resulting lack of information and justifications about their suitability and efficacy. Additionally, pre and post-augmentation need high-performance computational resources and time to produce the augmented image and evaluate the model performance. Thus, this study aims to develop a novel efficient augmentation approach for BUS images with advanced neural style transfer (NST) and Explainable AI (XAI) harnessing GPU-based parallel infrastructure. We scale and distribute the training of the augmentation model across 8 GPUs using the Horovod framework on a DGX cluster, achieving a 5.09 speedup while maintaining the model's accuracy. The proposed model is evaluated on 800 (348 benign and 452 malignant) BUS images and its performance is analyzed with other progressive techniques, using different quantitative analyses. The result indicates that the proposed approach can successfully augment the BUS images with 92.47% accuracy.

Introduction

The rising prominence of deep learning (DL) based techniques to be explainable is becoming more paramount, especially in domains where critical decisions must be made quickly, like medical image analysis. However, among all the cancers, breast malignancy (BM) is the most prevalent disease and is the fifth leading cause of cancer-related death among women worldwide (Atrey, Singh, and Bodhey 2024). As per the World Health Organization (WHO), in 2020, approximately 2.3 million new BM were reported with 6,85,000 deaths due to this disease. Further, according to the American Cancer Society in the United States, there will be 310,720 new cases were reported for BM and 56,500 cases of Ductal Carcinoma In Situ (DCIS) will be identified as of the year 2024. Therefore, early diagnosis of

BM may decrease the disease's effects, reduce the chance of infection, and improve medical treatment. In place of biopsy and physical examination, medical imaging (breast magnetic resonance imaging (MRI), mammogram, and, ultrasound (US), etc.) is an essential component in the timely detection of BM (Atrey et al. 2023; Panigrahi et al. 2024; Panigrahi, Verma, and Singh 2022). Although biopsy is the current gold standard procedure for BM diagnosis, due to the lack of labs in remote locations and, the painful, inconvenient, and time-consuming process, US imaging is an essential alternative in comparison to MRI and mammography for diagnosing BM. Also, when comparing MRI and mammography, the US has a number of advantages such as enhanced sensitivity, radiation-free imaging, cheap cost, and convenient accessibility (Panigrahi, Verma, and Singh 2019; Zhu et al. 2024; Panigrahi, Verma, and Singh 2018). However, due to significant drawbacks of US images like poor contrast and resolution, indistinct margins caused by noise such as speckles, faint surrounding tissue, and acoustic shadowing, the breast US (BUS) image-based diagnostic method is extremely operator-reliant.

To overcome these issues computer-aided detection (CAD) system using breast US images is introduced by the researcher (Zhu et al. 2024; Panigrahi, Verma, and Singh 2018; Rahmani, Shirazi, and Behnam 2024; Wang et al. 2024). In order to reduce operator dependency, inter and intra-observer variability and offer an alternate method for the automated and early BM diagnosis, the current CAD systems made use of machine learning (ML) and DL techniques (Panigrahi et al. 2024). Further, the performance of the DL models significantly depends on training data set size and requires human annotation by radiologists. The latter is a time-consuming task. Therefore, publicly accessible BUS image data sets are small resulting in over-fitting and unable to provide generalized output. Moreover, large BUS datasets are difficult to manage because of privacy and legal concerns. Hence, image augmentation is a necessary and challenging step to enhance the performance of the DL models and regularize the overfitting (Xu et al. 2024). Though existing DL models have achieved some success in this direction, their performance and suitability for augmentation in BUS images are still unsatisfactory (Oza et al. 2022). Further, most researchers use the traditional DL models as black-box models for image augmentation (Sarp et al. 2023). These

cutting-edge DL models lack of the information and justifications to support the radiologists for better decisions and interpretations of BM. This opportunity is made possible by explainable AI (XAI), which converts DL-based black-box models into more transparent and understandable gray-box models. Additionally, pre and post-augmentation need high-performance resources for computation and time to produce the augmented image and evaluate the model performance. Thus, integrated data-parallel distributed training on high-performance computing systems built with GPUs becomes essential (Masuma Iqrah et al. 2024; Koo et al. 2023).

This motivates us to develop a novel augmentation approach for BUS images with advanced Neural Style Transfer (NST) and XAI harnessing GPU-based parallel infrastructure. The proposed augmentation approach is three-fold such as 1) Initially we introduced a novel style loss function by combining the style loss from demystifying NST (DNST) (Li et al. 2017) and mr^2 NST (Wang et al. 2020) model, 2) further, A XAI based layer-wise relevance propagation (LRP) method is applied to the content loss function of the proposed NST model for explaining the importance of the features. This model is a post-hoc XAI model that computes the relevance score to indicate the significance of a feature in the input image, 3) To improve the efficiency of the augmentation model a distributed deep learning model training using Horovod framework on a DGX cluster that executes on 8 GPUs with a nearly linear speedup of 5.09 is used. Finally, the efficacy of the presented model is determined through quantitative analysis.

Contributions and paper outline

After identifying the shortcomings in current research (covered in), the following are the proposed approaches this study presents to address these issues:

- A novel NST-based augmentation model is proposed by combining the demystifying NST (DNST) (Li et al. 2017) and mr^2 NST (Wang et al. 2020) model. In this model the two loss components utilize a pre-trained ResNet50 model to extract semantic features from images as well as to resolve overfitting and gradient degradation issues.
- An XAI-based LRP method is integrated with the content loss function of the proposed augmentation model and a heatmap is generated to explain the importance of the extracted features for the model's decision-making process. By elucidating key features, this model aims to improve the interpretability and performance of the deep learning model, facilitating more generalized outputs.
- To improve the efficiency of the augmentation model, a distributed deep learning model training leveraging Horovod on a DGX is employed that executes on 8 GPUs, yielding 5-fold speed up compared to the single-GPU execution time.
- To classify pre and post-augmented BUS images, we utilized a fully fine-tuned ResNet50 model to improve the accuracy and to support the radiologists for better decisions and interpretations of breast malignancy. The ResNet50 trained with augmented data yields 92.47%

accuracy and it increased by 37.26% from the pre-augmented BUS images.

- To demonstrate the efficacy of the proposed model, we compared our model with cutting-edge methods using benchmark evaluation metrics.

The remaining paper is organized as follows. Section presents the related work and theoretical background on the augmentation model. Section , covered the materials and techniques utilized in the suggested methodology. The experimental results and discussions are described in Section , and finally, this study is wrapped up in Section .

Related work

In recent years, several studies have been published highlighting the image augmentation for medical imaging using the DL models. In Oza, P. (Oza et al. 2022), the author summarizes different types of image augmentation techniques for medical images. Generally, conventional image augmentation techniques utilize fundamental procedures to produce training images such as geometric transformation (e.g. flipping, rotation, translation, and scaling), pixel level augmentation (e.g., noise addition, sharpening), pseudo-color augmentation, random erasing, kernel filters (Xu et al. 2024). However, these techniques choose a transformation sequence at random for each image or depend on human professionals who have previous experience with the dataset to create a transformation sequence that will be used in training, which leads to training samples that are not sufficiently diverse. Thus, the researcher has proposed some advanced augmentation techniques such as generative adversarial networks (GAN) (Al-Dhabyani et al. 2019), neural style transfer (NST) (Georgievski 2019), SaliencyMix (Uddin et al. 2020), Random Erasing, and Keep Augment (Zhong et al. 2020). Though all of these techniques increase the model's accuracy, they are all limited by the incapacity of feedback changes in the model's accuracy to modify the image augmentation network. Therefore, figuring out which data augmentation technique best boosts the model's performance is challenging.

To overcome this problem Cubuk *et. al.* (Cubuk et al. 2019) proposed an automated search for improved data augmentation policies. This study maximizes the classifier's performance by automatically searching for a sequence of transformations. Though, this method lowers the classification error rate, simultaneously computationally intensive and time-consuming due to repeatedly training the sub-model enough with various augmentation rules. Nevertheless, each image has a different ideal set of modifications, thus few augmented images might not be helpful or even detrimental for training models (Xu et al. 2024). Further, to overcome this issue Xu *et. al.* (Xu et al. 2024) proposed an adaptive sequence-length-based deep reinforcement learning (ASDRL) model for autonomous data augmentation in medical image analysis. This study addresses issues like partially augmented images being insufficient and being ineffective by the automatic stopping mechanism (ASM) and the reward function with dual restrictions.

Another work by Georgievski *et al.* (Georgievski 2019) demonstrated image augmentation methods with NST. Later on, Ramadan *et al.* (Ramadan 2020) enhanced Convolutional Neural Network (CNN)’s effectiveness in BM detection in Mammograms images by combining data augmentation with a cheat sheet that included common features derived from region of interest (ROI), resulting in 12.2% and 2.2% increase in accuracy and precision respectively. However, there may be domain gaps between medical images collected from different modalities and suppliers and their highly distinctive visual styles, which might hamper DL models. Wang *et al.* (Wang et al. 2020) proposed a multi-resolution and multi-reference NST (mr^2 NST) network to address style variation in mammograms. Later on, Oza *et al.* (Oza et al. 2022) summarize the image augmentation methods for mammogram evaluation. In addition to the literature already mentioned, a few earlier works summarized the basic and advanced augmentation approaches in Table 1.

However, in literature various research works on high-performance computing systems (HPC) with GPUs are discussed to train the DL model such as this study (Sergeev and Del Balso 2018) introduced Horovod, an open-source library to train the DL models with large amounts of computation, that improves on both obstructions to scaling. Later on, Zhang, R. et. al. (Zhang, Cavallaro, and Jitsev 2020) proposed a distributed deep learning model using HPC with GPUs to speed up the learning of the unexplored low to high-resolution mapping of large volumes of Sentinel-2 image data. Further, this paper (Masuma Iqrah et al. 2024) used the Horovod-based distributed deep learning model to train a U-Net model, achieving a linear speedup of 7.21x using 8 GPUs.

Theoretical background

Transfer Learning based augmentation model Gatys *et al.* (Gatys, Ecker, and Bethge 2016) first introduced the NST. It aims to generate a stylized image \hat{I} using two input images: a content image I_c and a style reference image I_s . Then it proceeds to learn features from the content image through feature representations of $F_l(I_c)$ and $F_l(I_s)$ in layer l of an NST model. Each layer of feature maps, represented by $F_l(I)$, where $F_l \in R^{M_l(I) \times N_l}$ shows different aspects of style. Here, N_l denotes the number of feature maps in layer l , and $M_l(I) = H_l \times W_l(I)$ representing their spatial dimensions. The output image \hat{I} in NST is generated by minimizing a loss function shown in Eq. 1.

$$L_{total} = \alpha L_c(I_c) + \beta L_s(I_s) \quad (1)$$

where α and β represent as the weights of the style and content losses respectively. These two loss components utilize a pre-trained VGG19 model to extract semantic features from images. The L_c contrasts the feature maps of the \hat{I} and I_c defined in Eq. 2 and L_s contrasts the sum of summary statistics defined in Eq. 3.

$$L_c = \frac{1}{2} \sum_{i=1}^{N_l} \sum_{j=1}^{M_l} \left(F_{l_c}(\hat{I}) - F_{l_c}(I_c) \right)_{ij}^2 \quad (2)$$

SL. NO.	Augmentation approaches	Label Pre-serving	Pros	Cons
1	Geometric Transformation	No	Effective solution for the training data having positional bias and simple to implement.	Extra memory, computational cost is high for Transformation, computational time is more for training, and manual observation.
2	Noise Injection	Yes	Enables more robust learning of the model	It’s hard to decide the noise amount to be added.
3	Kernel Filters	Yes	Good for producing blurry and sharpened images	Comparable to the Constitutional Neural Network (CNN) approach.
4	Mixing Images	No	-	Unfit for use in medical imagery
5	Random Erasing	Not always	comparable to regularization for dropouts. Developed to overcome occlusion-related image identification difficulties, A promising method to ensure that a network looks at the whole image rather than just a portion of it.	Certain manual interventions can be required based on the application and dataset.
6	Adversarial Training	Yes	Assist in more effectively illuminating flimsy decision boundaries than conventional categorization metrics	Less investigation
7	Generative Adversarial Network	Yes	GANs produce data that resembles the source data.	Augmented data are more difficult to train.
8	Neural Style Transfer	-	Increases the simulated datasets capacity for generalization	Augmentation needs high-performance computational resources and time and the effort involved in choosing a style.

Table 1: Basic and advanced augmentation approaches (Oza et al. 2022).

$$L_s = \sum w_l E_l \quad (3)$$

where, in the layer l , w_l is the weight of the loss and E_l the squared error between the feature correlations provided by Gram matrices defined in Eq. 4. The Gram matrices $G_l(\hat{I})$ is the inner product between the feature map \hat{I} in layer l shown in Eq. 5.

$$E_l = \frac{1}{4N_l^2 M_l^2} \sum_{i=1}^{N_l} \sum_{j=1}^{N_l} \left(G_l(\hat{I}) - G_l(I_s) \right)_{ij}^2 \quad (4)$$

$$G_l(I) = \sum_{k=1}^{M_l} F_l(I)^T F_l(I) \quad (5)$$

However, according to (Li et al. 2017), the representation of style by the Gram matrix is unclear in the cutting-edge NST model. Thus, (Li et al. 2017) proposed a modified the L_{style} function by minimizing the Maximum Mean Discrepancy (MMD) (for detailed description about MMD please see Eq. 1, 2 and 8 in (Li et al. 2017)) using the second order polynomial kernel described in Eq. 6.

$$\begin{aligned} L_{MMDstyle} &= \frac{1}{4N_l^2 M_l^2} \sum_{k_1=1}^{M_l} \sum_{k_2=1}^{M_l} \left(k(f_{l \cdot k_1}, f_{l \cdot k_2}) \right. \\ &\quad \left. + k(f_{l(I_s) \cdot k_1}, f_{l(I_s) \cdot k_2}) \right) \quad (6) \\ &= \frac{1}{4N_l^2} MMD^2[F_l, F_l(I_s)] \end{aligned}$$

Though the NST model proposed in (Gatys, Ecker, and Bethge 2016) is a benchmarking method for image augmentation, it suffers from various limitations:

- support images with a resolution less than 1000×1000 . Due to the greater dimensions of the medical images like 2000×2000 , the degree of mild anomalies could be affected.
- The style reference image chosen manually for model input

To address the first shortcoming (Wang et al. 2020) used a multi-resolution model and for the second issue (Wang et al. 2020) study proposed multi-reference NST (mrNST) model shown in Eq. 7 and the necessary condition are shown in Eq. 8 and 9.

$$L_{multi-ref} = \sum w_l E_L \quad (7)$$

where,

$$E_l = \frac{1}{4N_l^2 M_l^2} \sum_{i=1}^{N_l} \sum_{j=1}^{N_l} \left(G_l(\hat{I}) - G_l \right)_{ij}^2 \quad (8)$$

$$G_l = H(M(F_l(I_{s_1}), F_l(I_{s_2}), \dots, F_l(I_{s_n})), \bar{h}) \quad (9)$$

The function $M()$ performs an element-wise max operation on a set of feature maps $F(I_{S_n})$ corresponding to the

n^{th} reference image at the l^{th} layer. These feature maps have dimensions of $nN_l \times H_l \times W_l$. The output of this operation is a square matrix G_l with dimensions $N \times N$. Each element g_{ij} is computed as the maximum value obtained from the corresponding elements across all feature maps. H is a histogram specification function and \bar{h} is the density histogram.

Layer-wise relevance propagation (LRP) LRP is a backward propagation method implemented for delivering explanations and performing exceptionally well across multiple benchmarks (Montavon, Samek, and Müller 2018). The LRP model is a post-hoc XAI model. In (Binder et al. 2016), the LRP method is extended to Neural Network (NN) that include local renormalization layers and a common product-type non-linearity found in DNN. Further, (Montavon, Samek, and Müller 2018) used the LRP method to offer theories, suggestions, and tips for utilizing it on actual data as effectively as possible. This study proves that gradient-based methods like LRP are more significant in detecting negatively relevant areas as compared with guided backpropagation.

Let R_j^{l+1} denote the relevance of neuron j at a network layer $l+1$ with respect to the prediction $f(x)$. Then, decompose R_j^{l+1} into message $R_{i \leftarrow j}^{(l, l+1)}$ sent to those neurons i at the preceding layer l to provide inputs to j which presented in Eq. 10.

$$R_j^{(l+1)} = \sum_{i \in (l)} R_{i \leftarrow j}^{(l, l+1)} \quad (10)$$

Similarly, the relevance of a neuron i at lower layer l accumulates all messages from the neurons in the higher layer $l+1$, described in Eq. 11.

$$R_i^{(l)} = \sum_{j \in (l+1)} R_{i \leftarrow j}^{(l, l+1)} \quad (11)$$

Based Eq. 12 the combination of the Eqs. 10 and 11 guarantees a conservation property of importance between layers. So, the chain of equalities is presented in Eq. 13

$$\sum_i R_i^{(l)} = \sum_i \sum_j R_{i \leftarrow j}^{(l, l+1)} = \sum_j \sum_i R_{i \leftarrow j}^{(l, l+1)} = \sum_j R_j^{(l+1)} \quad (12)$$

$$\sum_{k=1}^d R_k = \dots = \sum_i R_i^l = \sum_j R_j^{(l+1)} = \dots = f(x) \quad (13)$$

Origin of the problems

Though NST, mr^2 NST, and demystifying NST are the benchmarking methods for image augmentation, even so, they suffer from the following downsides.

- In mr^2 NST, the VGG19 model is used for augmentation as a result it suffers from the overfitting as well as vanishing gradient problem which makes the slower training process (Mascarenhas and Agarwal 2021; Li et al. 2020).
- E_l described in Eq. 8 does not clear the representation of style by the Gram matrix (Li et al. 2017).

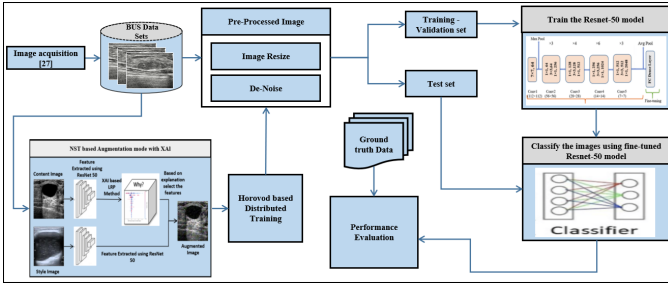


Figure 1: Workflow for the proposed model.

- $L_{MMD_{style}}$ described in Eq. 6 does not address style diversity in the images.
- The traditional DL models are black-box models and can not give enough context for the model's specifics (Sarp et al. 2023).
- Existing NST-based augmentation methods need high-performance computational resources and time and the effort involved in choosing a style image (Oza et al. 2022).
- It is difficult to compare new methodologies because there are no augmentation techniques that explain the model's specifics.

Material and Methods

This section provides a summary of the resources and techniques utilized in the different stages of BUS image augmentation and classification. The diagram illustrating the framework of the proposed model can be found in Fig. 1. Further, the augmentation block described in Fig. 1, is briefly presented in Fig. 2, which demonstrated how the proposed augmentation model was trained and tested. Initially, we combining the style loss from demystifying NST (DNST) and mr^2 NST model with ResNet50 and reformulate the style loss by using the second-order degree polynomial kernel for augmenting the images. Further, to explain the contributions of each input feature from the content images we utilized the LRP technique. This technique calculates relevance scores by utilizing the activation of each layer. These scores serve to highlight the significance of individual pixels or features within the input image toward generating the final output of the model. In the next step, we leveraged the Horovod framework to distribute the training of the proposed augmentation model, enabling scaling across an 8-GPU DGX cluster. This approach resulted in a significant acceleration, achieving a remarkable 5.09 speedup compared to single-GPU training. Further, we employed the SRAD filter in augmented BUS images to reduce the speckle noise. For each input image, this filter produces an illustration with several scales. As the scale progresses, the noise is systematically reduced, which enhances image clarity and quality. Next, we classify the denoised augmented images with a fine-tuned ResNet50 model to improve the classification accuracy. Finally, we compare our proposed XAI-based augmentation model with the existing cutting-edge augmentation methods.

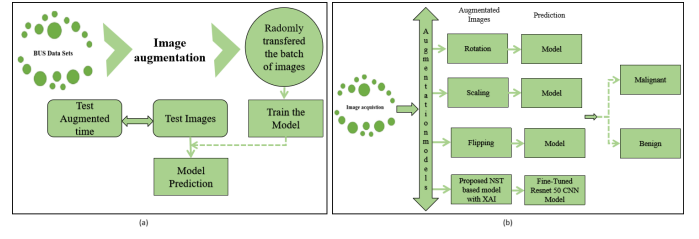


Figure 2: Training and testing of proposed image augmentation model.

Data demographics and preprocessing

The proposed model is evaluated on a publicly available database comprising 800 BUS images, of which 348 are benign and 452 are malignant. Among these images, 167 are sourced from a public repository The second dataset, obtained from (Al-Dhabyani et al. 2020), consists of 633 images.

The imaging instruments employed for scanning breast lesions are the LOGIQ E9 and the LOGIQ E9 Agile ultrasound systems, renowned for their high-quality imaging capabilities in radiology, cardiology, and vascular care, especially when it comes to the scanning of breast lesions. These devices, which have a resolution of $1280 * 1024$ pixels, provide clear images that are necessary for precise diagnosis. They make use of the ML6-15-D matrix linear probe's 1–5 MHz transducer.

Bus image filtering In medical imaging, particularly in BUS images, noise is a persistent issue that compromises the quality of extracted features. These images often suffer from speckle noise, leading to blurred edges, poor contrast, and reduced resolution, thereby preventing the effectiveness of CAD systems. To address this challenge, denoising is a crucial step. In this research, we employ the SRAD filter (Panigrahi et al. 2024; Panigrahi, Verma, and Singh 2019, 2022) to diminish noise and speckle across at different levels, producing a multi-scale image series. The selection of SRAD is deliberate because it effectively reduces noise while preserving texture information by halting diffusion across sharp edges as well as making an illustration in several scales for every image such that the noise consistently decreases with increasing scale. This approach aims to enhance the diagnostic accuracy and overall performance of CAD systems in analyzing BUS images.

Proposed augmentation model

Proposed style loss function In this proposed model, by enlarging Eq. 4, we obtained Eq. 17. Further, we reconstructed the style loss function given in Eq. 3, by combining $L_{MMD_{style}}$ in Eq. 6 and $L_{multi-ref}$ in Eq. 7 and 8. The proposed L_{ps} presented in Eq. 14.

$$L_{ps} = \frac{1}{4N_l^2} MMD^2 \sum_{ij} ([F_l, F_l(I_s)])_{ij}^2 \quad (14)$$

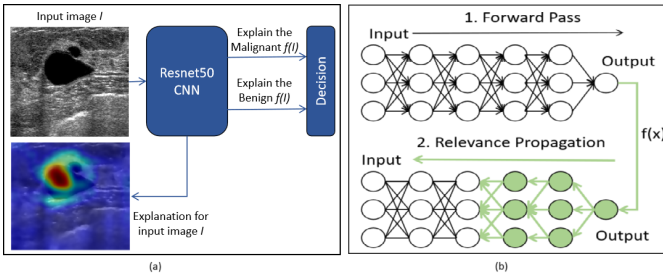


Figure 3: (a) Explanation of the prediction $f(I)$ for a given image I and (b) architecture of LRP method.

LRP propagation in ResNet50 model Let the neurons of the CNN, represented by the Eq. 15.

$$a_{i,j,k} = \sigma \left(\sum_{m=1}^M \sum_{n=1}^N \sum_{c=1}^C w_{m,n,c,k} a_{i+m-1,j+n-1,c} + b_k \right) \quad (15)$$

where, the activation of neuron $a_{i,j,k}$ is represented at the position (i,j) . Position in the k^{th} feature map, m and n represent the height and width of the kernel respectively, $a_{i+m-1,j+n-1,c}$ neuron activation of the previous layer, b_k and $w_{m,n,c,k}$ are the bias and weight of the neuron, and σ is the activation function.

LRP aims to assign a relevance score R_p to each pixel p in a given content image of x in conjunction with a predictor function f such that $f(x) \approx \sum_p R_p$. The $R_p > 0$ represents the pixel, positively contributes to the output and $R_p < 0$ indicates the negative contributes to the output. The pictorial representation of this score is presented as an image named a heatmap and the architecture of the LRP method is demonstrated in Fig. 3 (a) and Fig. 3 (b) respectively.

Additionally, the Eq. 15 constituted with α - β rule for formulating the messages $R_{i \leftarrow j}^{(l,l+1)}$ (discussed in Sec) shown in Eq. 16.

$$R_{i+M-1,j+n-1,c}^{(l,l+1)} = \sum_{i,j,k} \left(\alpha \frac{a_{i+m-1,j+n-1,c} w_{m,n,c,k}^+}{\sum_{m',n',c'} a_{i+m'-1,j+n'-1,c'} w_{m',n',c',k}^+} - \beta \frac{a_{i+m-1,j+n-1,c} w_{m,n,c,k}^-}{\sum_{m',n',c'} a_{i+m'-1,j+n'-1,c'} w_{m',n',c',k}^-} \right) R_{i,j,k}^{(l)} \quad (16)$$

where, $()^+$ and $()^-$ presents the positive and negative score respectively.

Distributed augmented model training using Horovod Framework The training of our augmentation model is computationally intensive, necessitating a focus on distributed training to enhance scalability. To this end, we employed synchronized data parallelism to facilitate the scaling of the augmentation model training across multiple GPUs.

To make our single-GPU implementation to a Horovod-based multi-GPU distributed training framework, we pursued the following steps:

We began by initializing Horovod with the function `hvd.init()`, subsequently assigning a GPU to each of the TensorFlow processes. Then we encapsulated the TensorFlow optimizer within the Horovod optimizer using the command `opt = hvd.DistributedOptimizer(opt)`. This Horovod optimizer is responsible for managing gradient averaging through a ring-based all-reduce mechanism. Finally, we synchronized the initial variable states by broadcasting them from the rank 0 process to all other processes using the `hvd.callbacks.BroadcastGlobalVariablesCallback(0)` method. These steps ensured that our model training is efficiently distributed across multiple GPUs, thereby improving scalability and performance.

Classification and performance evaluation of augmented images

A model's performance can be improved while requiring less intensive training and careful data annotation when it is fine-tuned. It is in the classification of medical images (Davila, Colan, and Hasegawa 2024) where the images are usually complex, sparse such as BUS images. According to the classification results presented in (Davila, Colan, and Hasegawa 2024) the fine-tuned ResNet50 model has certain advantages over other benchmark techniques. Therefore, a fine-tuned ResNet50 (Davila, Colan, and Hasegawa 2024; Hossain et al. 2022) is employed in this research for classifying augmented images. However, the existing fine-tuned ResNet50 model is trained with different image datasets such as ImageNet and other medical images. Thus, in this study to classify the pre and post augmented images, we employed a ResNet50 architecture. Initially, we split the image data set into train, validation, and test sets. Then, trained the ResNet50 model with the BUS images (discussed in). For breast cancer classification, we applied full fine-tuning since pretrained features from ImageNet are not optimal, and the distribution shift is minimal. By tuning all layers with the new data, the model can adapt and learn specific features (e.g., textures, patterns, abnormalities) from breast images, generally resulting in improved performance metrics (accuracy, precision, recall). Further, for the performance evaluation we used Eqs. (8)-(13) from (Panigrahi et al. 2024) to assess the performance of the classification model using different metrics.

Experimental results and discussion

Experimental setup and Evaluation Metrics

This section presents a detailed description of the experimental setup used and performance evaluation of the proposed augmentation model along with the classification of augmented data for BUS images. All experiments were executed utilizing Python, MATLAB R2024a, and Dev C++, operating on a Dell laptop furnished with a 13th Generation Intel(R) Core(TM) i9-13900HX processor clocked at 2.20 GHz, paired with 16 GB of RAM. Further, to speed up the model an NVIDIA DGX A100 machine is equipped with dual CPUs, each hosting four A100 GPUs is used.

This study utilized two variations of the ResNet50 model: the first is a pre-trained ResNet50 used for augmenting the

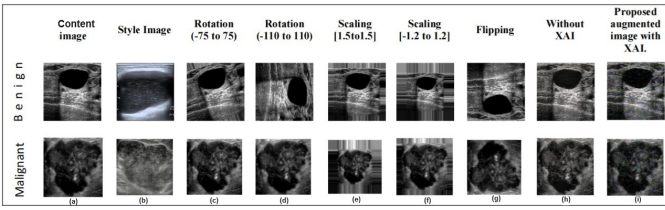


Figure 4: Implementation of different geometric and advanced image augmentation techniques.

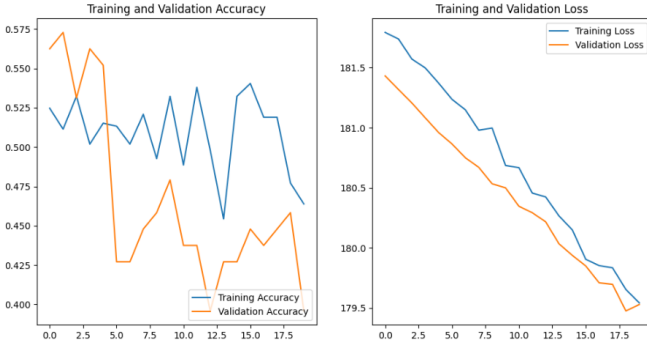


Figure 5: Classification model performance before augmentation.

BUS images, and the second is a fully fine-tuned ResNet50 utilized to classify the datasets, where, the dataset were split into 70% training, 15% validation, and 15% test set for both before and after augmentation as shown in Fig. 1.

We collected a dataset comprising 800 BUS images. Further, to illustrate the optimal balance between minimizing noise and retaining texture details, we applied the SRAD filter with parameters set to an iteration interval of $n_t = 10$ and a number of scales $L = 8$. The implementation of the SRAD filter was carried out using MATLAB and DEV C++. Following the denoising process, a fully fine-tuned ResNet50 classifier is employed to classify the BUS images. Since the existing ResNet50 classifier model was trained with ImageNet datasets, thus we trained the ResNet50 model with the BUS images and found a classification accuracy of 55.21%. The lower accuracy is due to overfitting. To resolve this issue, we implemented a novel XAI-based NST augmentation model on the original image.

XAI-based NST augmented model training using Horovod framework

This augmentation process unfolds in three distinct phases, outlined as follows:

Step 1: The style loss function of the NST model is designed by combining $L_{MMDstyle}$ and $L_{multi-ref}$. This is not only clear the representation of style by the Gram matrix but also addresses style diversity in the images. In the proposed augmentation model the weight w_l is set as 1.0 and the no of iteration is set as 1000, the loss function α and β in Eq. 1 is set as 1 (since the content losses from vari-

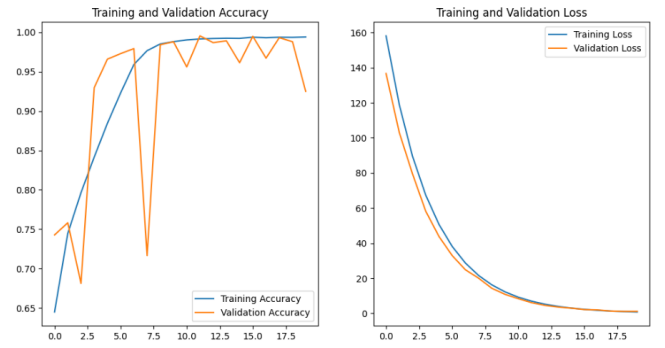


Figure 6: Classification model performance after proposed XAI-based augmentation.

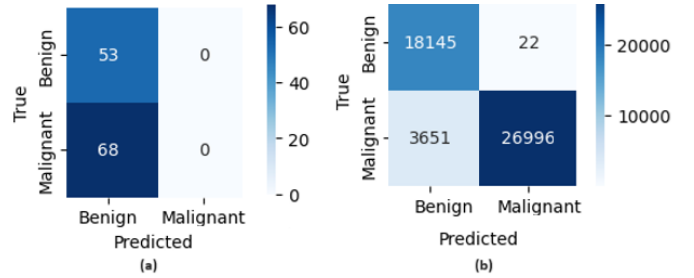


Figure 7: (a) and (b) are the confusion matrix of the classification model before and after augmentation respectively.

ous approaches are same) and $\gamma\beta'$ (to maintain the balance between content and style matching) respectively and used ResNet50 in place of Vgg19 for extract the features from content and style images.

Step 2: Propagate the LRP method in the ResNet50 model to explain the contributions of each input feature from the content images.

Step 3: To address the computational intensity of the XAI-based augmentation method we have utilized a distributed training approach leveraging Horovod that evenly split the content images among the GPUs where each process works on its subsets. For this, we have applied an NVIDIA DGX A100 machine equipped with dual CPUs, each hosting four A100 GPUs.

To prove the efficacy of the augmentation model we compare our model with other cutting-edge methods shown in Fig. 4. Figs. 4 (a) and (b) show the content and style image samples of benign and malignant images respectively. Figs. 4 (c)-(g) represents the results of geometric augmentation methods like rotation, scaling, and flipping respectively. Figs. 4 (h) and (i) show the augmented results by a proposed NST model without XAI and with XAI.

To determine the efficient improvement in the augmentation model Table 2 presents the pre and post augmentation dataset size and model performance in terms of accuracy. It is observed that the specified augmentation model is not only able to increase the data size from 800 to 325,408 but also enhance the accuracy by 37.26% as a result the model solved the overfitting issue as well as the vanishing gradient

Aug model	sub category	Pre-aug Dataset Size	Post-aug Dataset Size	Post-aug model performance
Geometric Transform (Kalaivani, Asha, and Gayathri 2023)	Rotation	800	4000	Improved by 13 Increased by 15 Raised by 12
	Scaling	800	4000	
	Flipping	800	4000	
NST with Vgg19 (Kavitha et al. 2021)	-	800	800	Improved by 13
mr^2 NST (Wang et al. 2020)	-	800	1600	Improved by 17
Proposed NST method without XAI	-	800	325,408	Enhanced by 20
Proposed NST method with XAI (LRP)	-	800	325,408	Enhanced by 37.26

Table 2: Pre and post-augmentation dataset scaling impact on model accuracy (%).

No of process	Parallel Time (Sec)	Sequential Time (Sec)	Speedup
	T_p	T_s	$S=T_p/T_s$
1	3771.53	3771.53	1
2	1953.60		1.93
4	1166.73		3.23
6	847.10		4.45
8	739.65		5.09

Table 3: Multiprocessor based Augmentation model.

problem which makes faster the training process.

Horovod framework: To enhance the computational efficiency of the augmentation model, parallelization is employed. This made it possible for the process to be carried out more quickly. We observed a notable acceleration of up to 5.09 times in a parallel computing environment when compared to a sequential operation. We were able to generate 325,408 images in a total of 739.65 seconds with 8 GPUs. Table 3 displays the acceleration in performance and the duration of parallel processing for this task, respectively.

Quantitative evaluation of ResNet50 model for augmented image classification

In this section, we present the numerical findings derived from the proposed augmentation model. Additionally, we performed a comparative analysis between the outcomes of our presented approach and those of currently available

Augmentation method	sub category	Acc	Recall	Specif-icity	Preci-sion	F1-score
Geometric Transform (Kalaivani, Asha, and Gayathri 2023)	Rotation	83.06	82.01	82.33	83.56	82.78
	Scaling	85.48	84.22	84.11	85.43	84.79
	Flipping	81.45	80.27	80.67	81.55	80.86
NST with Vgg19 (Kavitha et al. 2021)	-	83.34	82.70	81.33	83.11	82.92
mr^2 NST (Wang et al. 2020)	-	89.23	87.45	87.78	88.61	88.08
Proposed NST method without XAI	-	90.71	91.34	92.45	90.45	90.84
Proposed NST method with XAI (LRP)	-	92.47	94.11	99.88	92.50	93.20

Table 4: Quantitative evaluations for augmentation algorithms (%)

augmentation techniques. The associated quantitative results are highlighted in Table 4, showcasing various performance metrics including accuracy (Acc), recall, specificity, precision, and F1-Score.

A fully fine-tuned ResNet50 (trained by the collected BUS dataset) is used to classify the augmented images and evaluate the model performance. Using the proposed augmentation approach the data size was expanded to 325,408 images (121,104 benign and 204,304 malignant). Further, these augmented images are following the same pre-processing steps as before augmentation, including SRAD filtering, and were then split into training, testing, and validation sets, and classified using fully fine-tuned ResNet50. To achieve optimal performance and improved classification accuracy, the proposed model was trained for 20 epochs using early stopping after 7 consecutive epochs without validation loss improvement. We utilized the LeakyRelu activation function (due to accepting negative input), SGD optimizer with an initial $\eta = 0.0001$ and momentum = 0.9, which subsequently reduced by *ReduceLROnPlateau* function to enhance convergence. To ensure consistency, compatibility, and future scalability, *categorical cross-entropy* with one-hot encoding is employed. A batch size of 32 is chosen to balance GPU memory efficiency and parallelization. To prevent overfitting and optimize training, we incorporated dropout (0.5) and batch normalization. A *GlobalAveragePooling2D* is used to connect the layers, followed by a final dense layer with 2 units and softmax activation for classification.

Fig. 5 and 6 present classification model performance before and after augmentation respectively. Fig. 5 shows that before augmentation the model struggles with learning, showing instability in accuracy and only minimal decreases in loss, suggesting that augmentation plays a critical role in improving model performance. However, Fig. 6 shows significant improvements, with high and stable accuracy and rapidly decreasing loss, indicating effective learning and good generalization. Further, before augmentation, the model archives a training and validation accuracy of 46.39% and 39.58% whereas, after augmentation training and validation accuracy improved to 99.38%, and 92.49% respectively and the test dataset resulted in a test accuracy of 92.47%.

We examine the confusion matrix of benign, and malignant for the ResNet50 classification models shown in Fig. 7. Fig. 7 (a) shows that before augmentation 53 samples were correctly classified as benign and 68 samples were incorrectly classified as malignant rest of the part are 0. Whereas, Fig. 7 (b) shows a more balanced performance after augmentation, with a significant number of correct predictions for both benign and malignant cases.

The performance of several augmentation models in terms of ACC, recall, specificity, precision, and F1-score is presented in Table 4. It can be noticed that this study obtained higher accuracy due to the L_{ps} being applied along with LRP. The aim of using LRP is the conservation principle and ability to identify the negatively relevant. This technique calculates relevance scores by utilizing the activation of each layer. These scores serve to highlight the significance of individual pixels or features within the input image towards generating the final output.

Conclusion

In this paper, we have introduced an innovative augmentation model which automatically augments the BUS images. This paper addresses the limitations of demystifying NST (DNST) and mr^2 NST method by the proposed objective function and gives the context for the model's specifics. Furthermore, it enhances efficiency by leveraging Horovod across multiple GPUs, significantly reducing computational time. We demonstrate that, when compared with other standard augmentation techniques, the suggested model outperforms better and is more precise. The results of our experiments demonstrate the superior accuracy and effectiveness of the proposed model over existing benchmark augmentation algorithms.

This study can be enhanced in the future in a number of ways, including (1) Evaluation on larger datasets to strengthen confidence in performance, (2) Soliciting expert input to further enhance results, (3) Exploring the application of our technique to 3-D BUS images for improved the classification accuracy and performance of the CAD system.

References

Al-Dhabyani, W.; Gomaa, M.; Khaled, H.; and Aly, F. 2019. Deep learning approaches for data augmentation and clas-

sification of breast masses using ultrasound images. *Int. J. Adv. Comput. Sci. Appl.*, 10(5): 1–11.

Al-Dhabyani, W.; Gomaa, M.; Khaled, H.; and Fahmy, A. 2020. Dataset of breast ultrasound images. *Data in brief*, 28: 104863.

Atrey, K.; Singh, B. K.; and Bodhey, N. K. 2024. Multimodal classification of breast cancer using feature level fusion of mammogram and ultrasound images in machine learning paradigm. *Multimedia Tools and Applications*, 83(7): 21347–21368.

Atrey, K.; Singh, B. K.; Bodhey, N. K.; and Pachori, R. B. 2023. Mammography and ultrasound based dual modality classification of breast cancer using a hybrid deep learning approach. *Biomedical Signal Processing and Control*, 86: 104919.

Binder, A.; Montavon, G.; Lapuschkin, S.; Müller, K.-R.; and Samek, W. 2016. Layer-wise relevance propagation for neural networks with local renormalization layers. In *Artificial Neural Networks and Machine Learning—ICANN 2016: 25th International Conference on Artificial Neural Networks, Barcelona, Spain, September 6-9, 2016, Proceedings, Part II 25*, 63–71. Springer.

Cubuk, E. D.; Zoph, B.; Mane, D.; Vasudevan, V.; and Le, Q. V. 2019. Autoaugment: Learning augmentation strategies from data. In *Proceedings of the IEEE/CVF conference on computer vision and pattern recognition*, 113–123.

Davila, A.; Colan, J.; and Hasegawa, Y. 2024. Comparison of fine-tuning strategies for transfer learning in medical image classification. *Image and Vision Computing*, 146: 105012.

Gatys, L. A.; Ecker, A. S.; and Bethge, M. 2016. Image style transfer using convolutional neural networks. In *Proceedings of the IEEE conference on computer vision and pattern recognition*, 2414–2423.

Georgievski, B. 2019. Image Augmentation with Neural Style Transfer. In *International Conference on ICT Innovations*, 212–224. Springer.

Hossain, M. B.; Iqbal, S. H. S.; Islam, M. M.; Akhtar, M. N.; and Sarker, I. H. 2022. Transfer learning with fine-tuned deep CNN ResNet50 model for classifying COVID-19 from chest X-ray images. *Informatics in Medicine Unlocked*, 30: 100916.

Kalaivani, S.; Asha, N.; and Gayathri, A. 2023. Geometric transformations-based medical image augmentation. In *GANs for Data Augmentation in Healthcare*, 133–141. Springer.

Kavitha, S.; Dhanapriya, B.; Vignesh, G. N.; and Baskaran, K. 2021. Neural style transfer using vgg19 and alexnet. In *2021 International Conference on Advancements in Electrical, Electronics, Communication, Computing and Automation (ICAECA)*, 1–6. IEEE.

Koo, Y.; Xie, H.; Mahmoud, H.; Iqrah, J. M.; and Ackley, S. F. 2023. Automated detection and tracking of medium-large icebergs from Sentinel-1 imagery using Google Earth Engine. *Remote Sensing of Environment*, 296: 113731.

- Li, W.; Wang, Z.; Wang, Y.; Wu, J.; Wang, J.; Jia, Y.; and Gui, G. 2020. Classification of high-spatial-resolution remote sensing scenes method using transfer learning and deep convolutional neural network. *IEEE Journal of Selected Topics in Applied Earth Observations and Remote Sensing*, 13: 1986–1995.
- Li, Y.; Wang, N.; Liu, J.; and Hou, X. 2017. Demystifying neural style transfer. *arXiv preprint arXiv:1701.01036*.
- Mascarenhas, S.; and Agarwal, M. 2021. A comparison between VGG16, VGG19 and ResNet50 architecture frameworks for Image Classification. In *2021 International conference on disruptive technologies for multi-disciplinary research and applications (CENTCON)*, volume 1, 96–99. IEEE.
- Masuma Iqrah, J.; Wang, W.; Xie, H.; and Prasad, S. 2024. A Parallel Workflow for Polar Sea-Ice Classification using Auto-labeling of Sentinel-2 Imagery. *arXiv e-prints*, arXiv:2403.
- Montavon, G.; Samek, W.; and Müller, K.-R. 2018. Methods for interpreting and understanding deep neural networks. *Digital signal processing*, 73: 1–15.
- Oza, P.; Sharma, P.; Patel, S.; Adedoyin, F.; and Bruno, A. 2022. Image augmentation techniques for mammogram analysis. *journal of imaging*, 8(5): 141.
- Panigrahi, L.; Chandra, T. B.; Srivastava, A. K.; Varshney, N.; Singh, K. U.; and Mahato, S. 2024. mBCCf: Multilevel Breast Cancer Classification Framework Using Radiomic Features. *International Journal of Intelligent Systems*, 2024.
- Panigrahi, L.; Verma, K.; and Singh, B. K. 2018. Hybrid segmentation method based on multi-scale Gaussian kernel fuzzy clustering with spatial bias correction and region-scalable fitting for breast US images. *IET Computer Vision*, 12(8): 1067–1077.
- Panigrahi, L.; Verma, K.; and Singh, B. K. 2019. Ultrasound image segmentation using a novel multi-scale Gaussian kernel fuzzy clustering and multi-scale vector field convolution. *Expert Systems with Applications*, 115: 486–498.
- Panigrahi, L.; Verma, K.; and Singh, B. K. 2022. Evaluation of image features within and surrounding lesion region for risk stratification in breast ultrasound images. *IETE Journal of Research*, 68(2): 935–946.
- Rahmani, A. A.; Shirazi, A. A. B.; and Behnam, H. 2024. Automatic breast mass segmentation in ultrasound images with U-Net and resolution enhancement blocks. *Biomedical Signal Processing and Control*, 94: 106270.
- Ramadan, S. Z. 2020. Using convolutional neural network with cheat sheet and data augmentation to detect breast cancer in mammograms. *Computational and Mathematical Methods in Medicine*, 2020.
- Sarp, S.; Catak, F. O.; Kuzlu, M.; Cali, U.; Kusetogullari, H.; Zhao, Y.; Ates, G.; and Guler, O. 2023. An XAI approach for COVID-19 detection using transfer learning with X-ray images. *Heliyon*, 9(4).
- Sergeev, A.; and Del Balso, M. 2018. Horovod: fast and easy distributed deep learning in TensorFlow. *arXiv preprint arXiv:1802.05799*.
- Uddin, A.; Monira, M.; Shin, W.; Chung, T.; Bae, S.-H.; et al. 2020. Saliencymix: A saliency guided data augmentation strategy for better regularization. *arXiv preprint arXiv:2006.01791*.
- Wang, J.; Liu, G.; Liu, D.; and Chang, B. 2024. MF-Net: Multiple-feature extraction network for breast lesion segmentation in ultrasound images. *Expert Systems with Applications*, 123798.
- Wang, S.; Huo, J.; Ouyang, X.; Che, J.; Xue, Z.; Shen, D.; Wang, Q.; and Cheng, J.-Z. 2020. mr NST: Multi-resolution and Multi-reference Neural Style Transfer for Mammography. In *International Workshop on PRedictive Intelligence In MEDicine*, 169–177. Springer.
- Xu, Z.; Wang, S.; Xu, G.; Liu, Y.; Yu, M.; Zhang, H.; Lukasiewicz, T.; and Gu, J. 2024. Automatic data augmentation for medical image segmentation using Adaptive Sequence-length based Deep Reinforcement Learning. *Computers in Biology and Medicine*, 169: 107877.
- Zhang, R.; Cavallaro, G.; and Jitsev, J. 2020. Super-resolution of large volumes of sentinel-2 images with high performance distributed deep learning. In *IGARSS 2020-2020 IEEE International Geoscience and Remote Sensing Symposium*, 617–620. IEEE.
- Zhong, Z.; Zheng, L.; Kang, G.; Li, S.; and Yang, Y. 2020. Random erasing data augmentation. In *Proceedings of the AAAI conference on artificial intelligence*, volume 34, 13001–13008.
- Zhu, C.; Chai, X.; Wang, Z.; Xiao, Y.; Zhang, R.; Yang, Z.; and Feng, J. 2024. DBL-Net: A dual-branch learning network with information from spatial and frequency domains for tumor segmentation and classification in breast ultrasound image. *Biomedical Signal Processing and Control*, 93: 106221.

Rephrasing the style loss function

$$\begin{aligned}
L_s &= \frac{1}{4N_l^2 M_l^2} \sum_{i=1}^{N_l} \sum_{j=1}^{N_l} \left(\sum_{k=1}^{M_l} F_{l_i k}(I)^T F_{l_j k}(I) - \sum_{k=1}^{M_l} G_{l_{ik}}(I_{s_{ik}}) G_{l_{jk}}(I_{s_{jk}}) \right)^2 \\
&= \frac{1}{4N_l^2 M_l^2} \sum_{i=1}^{N_l} \sum_{j=1}^{N_l} \left(\left(\sum_{k=1}^{M_l} F_{l_i k}(I)^T F_{l_j k}(I) \right)^2 + \left(\sum_{k=1}^{M_l} G_{l_{ik}}(I_{s_{ik}}) G_{l_{jk}}(I_{s_{jk}}) \right)^2 - \right. \\
&\quad \left. 2 \left(\sum_{k=1}^{M_l} F_{l_i k}(I)^T F_{l_j k}(I) - \sum_{k=1}^{M_l} G_{l_{ik}}(I_{s_{ik}}) G_{l_{jk}}(I_{s_{jk}}) \right) \right) \\
&= \frac{1}{4N_l^2 M_l^2} \sum_{i=1}^{N_l} \sum_{j=1}^{N_l} \sum_{k_1=1}^{M_l} \sum_{k_2=1}^{M_l} (F_{l_i k_1}(I)^T F_{l_j k_1}(I) F_{l_i k_2}(I)^T F_{l_j k_2}(I) + \\
&\quad G_{l_{ik_1}}(I_{s_{ik_1}}) G_{l_{jk_1}}(I_{s_{jk_1}}) G_{l_{ik_2}}(I_{s_{ik_2}}) G_{l_{jk_2}}(I_{s_{jk_2}}) - \\
&\quad 2 F_{l_i k_1}(I)^T F_{l_j k_1}(I) G_{l_{ik_2}}(I_{s_{ik_2}}) G_{l_{jk_2}}(I_{s_{jk_2}})) \\
&= \frac{1}{4N_l^2 M_l^2} \sum_{k_1=1}^{M_l} \sum_{k_2=1}^{M_l} \sum_{i=1}^{N_l} \sum_{j=1}^{N_l} (F_{l_i k_1}(I)^T F_{l_j k_1}(I) F_{l_i k_2}(I)^T F_{l_j k_2}(I) + \\
&\quad G_{l_{ik_1}}(I_{s_{ik_1}}) G_{l_{jk_1}}(I_{s_{jk_1}}) G_{l_{ik_2}}(I_{s_{ik_2}}) G_{l_{jk_2}}(I_{s_{jk_2}}) - \\
&\quad 2 F_{l_i k_1}(I)^T F_{l_j k_1}(I) G_{l_{ik_2}}(I_{s_{ik_2}}) G_{l_{jk_2}}(I_{s_{jk_2}})) \\
&= \frac{1}{4N_l^2 M_l^2} \sum_{k_1=1}^{M_l} \sum_{k_2=1}^{M_l} \left(\left(\sum_{i=1}^{N_l} F_{l_i k_1}(I)^T F_{l_i k_2}(I)^T \right)^2 + \left(\sum_{i=1}^{N_l} G_{l_{ik_1}}(I_{s_{ik_1}}) G_{l_{ik_2}}(I_{s_{ik_2}}) \right)^2 - \right. \\
&\quad \left. 2 (F_{l_i k_1}(I)^T G_{l_{ik_2}}(I_{s_{ik_2}}))^2 \right) \\
&= \frac{1}{4N_l^2 M_l^2} \sum_{k_1=1}^{M_l} \sum_{k_2=1}^{M_l} \left((F_{l_{k_1}}(I)^T F_{l_{k_2}}(I))^2 + (G_{l_{k_1}}(I_{s_{k_1}})^T G_{l_{k_2}}(I_{s_{k_2}}))^2 - 2 (F_{l_{k_1}}(I)^T G_{l_{k_2}}(I_{s_{k_2}}))^2 \right)
\end{aligned}$$

(17)